

Article

Temperature-Dependent Optical Properties of Bismuth Triborate Crystal in the Terahertz Range: Simulation of Terahertz Generation by Collinear Three-Wave Mixing in the Main Crystal Planes

Dmitry Ezhov ^{1,*}, Nazar Nikolaev ^{2,3}, Valery Antsygin ², Sofia Bychkova ², Yury Andreev ⁴ and Valery Svetlichnyi ^{1,*}

- ¹ Laboratory of Advanced Materials and Technology, Siberian Physical Technical Institute, Tomsk State University, Tomsk 634050, Russia
- ² Laboratory of Terahertz Photonics, Institute of Automation and Electrometry, Siberian Branch of the Russian Academy of Sciences, Novosibirsk 630090, Russia; nazar@iae.nsk.su (N.N.); antsign@iae.nsk.su (V.A.)
- ³ Laboratory of Laser Biophysics, Institute of Laser Physics, Siberian Branch of the Russian Academy of Sciences, Novosibirsk 630090, Russia
- ⁴ Laboratory of Geosphere-Biosphere Interactions, Institute of Monitoring of Climatic and Ecological Systems, Siberian Branch of the Russian Academy of Sciences, Tomsk 634055, Russia; yuandreev@yandex.ru
- * Correspondence: ezhov_dm@phys.tsu.ru (D.E.); v_svetlichnyi@bk.ru (V.S.)

Abstract: Terahertz (THz) frequency generation via nonlinear optical techniques is of particular interest due to the immense potential of this type of radiation in various scientific fields, ranging from medicine to telecommunications. Selecting suitable nonlinear media for laser frequency down-conversion presents a challenging task. Considering an approach that uses nonlinear crystals with high radiation resistance, pumped by intense laser pulses near their damage threshold, we suggest the crystal of bismuth triborate (BiB_3O_6 , BIBO). Compared to other borate-class crystals, BIBO exhibits relatively high coefficients of quadratic susceptibility. In this paper, we have studied the optical properties of BIBO samples in a wide spectral range from 0.1 to 2.1 THz at temperatures of 473, 383, 295, and 77 K using Terahertz Time-Domain Spectroscopy (THz-TDS). Furthermore, we simulated collinear three-wave interactions with nonzero efficiency for difference frequency generation (DFG) in the THz range. For the pump wavelengths of about 800 nm, we determined phase-matching (PM) conditions and compared the generation efficiency for different crystal cuts. The potential of utilizing BIBO crystal for terahertz frequency generation is discussed.

Keywords: bismuth triborate; terahertz frequency; refractive index; absorption coefficient; temperature dependencies; three-wave interactions; THz frequency generation; phase matching



Citation: Ezhov, D.; Nikolaev, N.; Antsygin, V.; Bychkova, S.; Andreev, Y.; Svetlichnyi, V.

Temperature-Dependent Optical Properties of Bismuth Triborate Crystal in the Terahertz Range: Simulation of Terahertz Generation by Collinear Three-Wave Mixing in the Main Crystal Planes. *Photonics* **2023**, *10*, 713. <https://doi.org/10.3390/photonics10070713>

Received: 5 May 2023

Revised: 16 June 2023

Accepted: 20 June 2023

Published: 22 June 2023



Copyright: © 2023 by the authors. Licensee MDPI, Basel, Switzerland. This article is an open access article distributed under the terms and conditions of the Creative Commons Attribution (CC BY) license (<https://creativecommons.org/licenses/by/4.0/>).

1. Introduction

The rapid development of terahertz (THz) technologies in recent decades in the field of biomedicine [1,2], monitoring and security systems [3], remote sensing of the atmosphere [4–6], wireless communications [7,8], and scientific research requires high-intensity and efficient radiation sources with the necessary spectral properties. There are numerous techniques for generating THz radiation, from classical radio-technical antenna devices to synchrotron sources. Devices based on photoconductive antennas or optical rectification in nonlinear crystals are widely used to solve many spectroscopic problems [9,10]. The approach based on phase-matched (PM) three-wave mixing or difference frequency generation (DFG) in nonlinear crystals has great potential for high-intensity, spectrally bright THz generation that is tunable in frequency over a wide range [11,12]. This approach is common for optical parametric generation in the infrared (IR) range [13].

The efficiency of DFG depends not only on the corresponding nonlinear susceptibilities but also on the number of properties of a nonlinear crystal, such as the laser damage threshold, absorption coefficients, birefringence, and group-velocity mismatch in different spectral ranges, PM conditions, and geometric dimensions. All these properties depend in a complex way on the pump radiation parameters, including the pump wavelength, pulse duration, beam spatial parameters, and initial pump beam intensity [14,15]. For example, in an LBO crystal that does not possess high nonlinear susceptibility, a record, up to 90%, energy efficiency of second-harmonic generation (SHG) was achieved at a pump intensity of 775 MW/cm^2 [16].

The first works devoted to DFG in the THz range considered semiconductor crystals with large nonlinear coefficients, such as ZnGeP_2 and GaSe, popular for parametric generation in the mid-IR range [17,18]. In recent years, oxygen-containing nonlinear crystals, for example, β -BBO, LBO, BBO, etc., have been considered for THz frequency generation [19–22]. They have much lower nonlinear coefficients, but, at the same time, possess laser-induced damage thresholds that are several orders of magnitude higher and a much lower absorption coefficient in the main transparency window. This fact should allow for the frequency conversion of high-peak-intensity emission from short-pulsed laser sources at visible wavelengths. The lower effective nonlinear coefficient and, hence, lower figure-of-merit (FOM) values compared to semiconductor crystals do not prevent the higher conversion efficiency since it is proportional to the pump intensity [23].

Among the known nonlinear crystals of the borate family, special attention should be paid to bismuth triborate, BiB_3O_6 (BIBO). BIBO is a positive biaxial crystal that belongs to the monoclinic crystal system, space group C2 [24]. Due to its chemical composition, structure, and mature growing technology, it has a low absorption coefficient and a high laser damage threshold ($>300 \text{ GW/cm}^2$ under 45 fs pump at 800 nm) in the visible and near-infrared spectral ranges occupied by powerful solid-state lasers (Nd:YAG, Ti:sapphire) [25,26]. Compared to other borate crystals, its nonlinear coefficients are approximately 4 and 1.7 times larger than those of the widely used LBO and β -BBO nonlinear crystals, respectively. These mark the BIBO crystal as an efficient device for an optical parametric generation of femtosecond pulses [27,28]. Furthermore, BIBO's linear absorption coefficient at the wavelength of 1064 nm is two times lower than that of the β -BBO crystal [29]. These properties make BIBO more attractive for high-intensity THz wave generation. In addition, the crystal is non-hygroscopic, thermally stable (has no phase transitions from 4 K and up to the melting point of 1019 K [30]), has sufficient hardness (5–6 on the Mohs scale), is good for optical polishing, and shows chemical stability, which is important for practical applications, especially in outdoor scenarios. To date, the terahertz optical properties of BIBO have not been studied in detail. Our preliminary study on absorption coefficients and refractive indices in the THz range for the principal optical axes of the crystal performed at room temperature allowed us to estimate possible PM conditions for DFG, revealing the prospects of BIBO [31,32]. To discover the full potential of the crystal for THz frequency generation, further verification is required.

A recently published article attempted to obtain THz generation from the BIBO crystal [33]. However, the authors used a sample that was cut for second-harmonic generation ($\theta = 28.9^\circ$). As a result, the registered THz generation output was likely inefficient, and the provided THz spectra were questionable and possibly misinterpreted.

In this work, the optical properties of the BIBO crystal were thoroughly studied in the THz range at different temperatures. The data obtained were used to simulate all possible PM conditions for collinear three-wave mixing, considering the THz radiation generation. We evaluated the efficiency and determined the optimal conditions for nonlinear conversion. This knowledge is crucial for the development of efficient and reliable nonlinear optical devices that employ BIBO crystals.

2. Materials and Methods

2.1. Properties of Samples under Test

We studied the THz optical properties of four BIBO crystal samples with a clear aperture diameter of 1 cm. Two samples were cut perpendicular to the dielectric y -axis and further referred to as y -cut samples with thicknesses of 526 and 5080 μm . The other two samples were x -cut with thicknesses of 518 and 5430 μm . Using additional thick samples allows us to measure absorption coefficients at a frequency range < 0.4 THz more accurately compared with the thin samples. The samples were obtained from Cstech[®], and their thicknesses were measured using a calibrated micrometer and refined using a measuring microscope. According to Cstech's inspection report, the samples were cut with an angle tolerance not exceeding $5'$ for thick samples and $10'$ for thin samples. Note that generally, for monoclinic point group 2 crystals, only one of the dielectric axes coincides with the crystallographic one. Thereby, the xyz frame rotates around one of the axes, and the angle depends on both wavelength and temperature [34]. Specifically, in the case of the BIBO crystal, the y - and z -axes rotate about the crystallographic b -axis, but their wavelength dependence does not exceed $\Delta\Phi = \pm 1^\circ$ in the main transparency window [29]. It is important to consider this fact when conducting polarimetry measurements to ensure accurate results. The arrangement of the dielectric (xyz), crystallophysical (XYZ), and crystallographic (abc) coordinate frames for the y -cut sample is depicted in Figure 1.

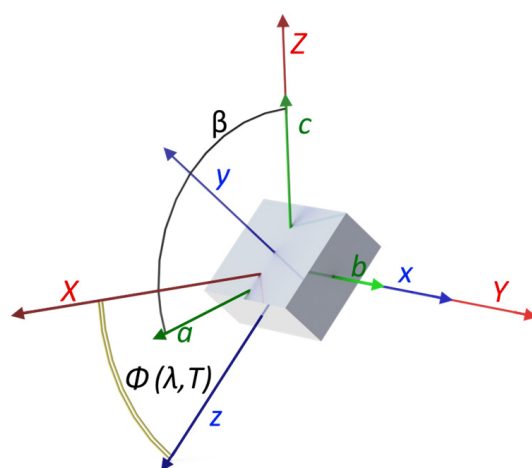


Figure 1. Mutual arrangement of the BIBO crystal coordinate frames in the y -cut sample.

2.2. Temperature-Dependent THz Polarimetry

Terahertz optical properties of the BIBO crystals were measured in the transmission geometry using manufactured in-house broadband THz-TDS, the scheme of which can be found in [35,36]. As a source of the femtosecond pulses, we used the emission of the second harmonic of the Er-doped fiber laser FFS-SHG (Toptica Photonics AG, Germany, Gräfelfing), with a mean power of 80 mW, central wavelength of 775 nm, and pulse duration of 130 fs. The THz waves were generated by an interdigitated large-area photoconductive antenna, iPCA-21-05-300-800-h (Batop, Germany, Jena), and detected utilizing the free space electro-optic sampling technique in a (110)-cut 2 mm thick ZnTe crystal. Samples were placed in a heating cell controlled by a PID regulator, TRM251 (Owen, Russia, Moscow), capable of maintaining the temperature with an accuracy of 0.1°C . To avoid a temperature gradient in the crystal, we preliminary measured the time required to establish thermal equilibrium in a heating cell using a calibrated thermocouple mounted on the surface of the sample under test before conducting THz measurements. The use of polytetrafluoroethylene windows covering the heating cell minimized temperature fluctuations caused by air drift. On average, it took about 10 min to establish temperature equilibrium.

The optical properties of two principal dielectric axes of the BIBO samples were measured without rotating and replacing the sample, following the procedure described in [37]. According to this technique, the sample under study was installed at an approximately 45° angle relative to the initial polarization of the THz field. The crystal’s principal axis of interest was selected by simultaneously rotating in concert two high-performance grid polarizers at ±45°.

Terahertz absorption coefficients and refractive indices of the samples under study were extracted from the time-domain signals using a technique described in [38].

3. Results

3.1. Optical Properties of BIBO Crystal in the THz Range at Room Temperature

The THz optical properties of the BIBO crystal were measured for both thick and thin samples at room temperature. The use of thin samples enabled the spectra to be acquired at frequencies higher than 1.5 THz, where the absorption coefficient exceeded the value of 10 cm⁻¹. Conversely, thick samples allowed us to obtain valid data in the frequency range below 0.5 THz, where the absorption coefficients were less than 0.1 cm⁻¹. By combining the spectra for both thicknesses of the samples, reliable data were obtained in the range of 0.1–2.1 THz. As a result, the extracted absorption coefficients and the refractive indices for the BIBO principal axes in a broad spectral range are shown in Figure 2.

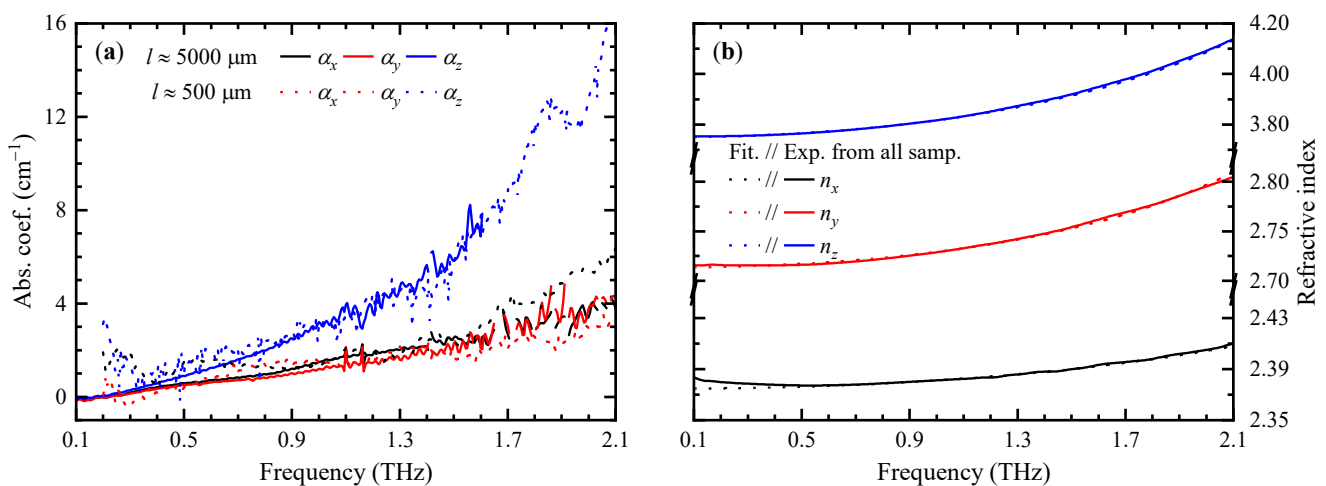


Figure 2. Optical properties of the BIBO crystal in the THz range at room temperature: (a) measured absorption coefficient of the crystal principal dielectric axes for two different sets of samples with thicknesses of 0.5 and 5 mm; (b) combined refractive indices of principle axes and their Sellmeier fitting.

The absorption coefficient along the dielectric z-axis varies from almost “0” cm⁻¹ (considering the measurement error) in the frequency region below 0.3 THz up to 16 cm⁻¹ at 2.1 THz. The absorption coefficients along the x- and y-axes were found to be practically similar to each other and increased slightly up to 4 cm⁻¹ at a frequency of 2.1 THz. The refractive index of the x-axis n_x slightly deviates upwards from a straight line in the frequency range below 0.4 THz. This deviation is most probably due to the Gouy phase shift of the focused THz wave in the thick (5 mm) sample, which, in our case, is not compensated by the spectra-processing algorithms [39]. Therefore, the data points in this range were omitted while fitting the curve with the Sellmeier equation. The final dispersion expressions for the principal axes of the BIBO crystal at room temperature are shown below:

$$\begin{aligned}
 n_x^2 &= 4.940 + \frac{0.700 \cdot \lambda^2}{\lambda^2 - 3777}, \\
 n_y^2 &= 6.372 + \frac{0.992 \cdot \lambda^2}{\lambda^2 - 7100}, \\
 n_z^2 &= 7.610 + \frac{6.456 \cdot \lambda^2}{\lambda^2 - 6515}.
 \end{aligned}
 \tag{1}$$

3.2. Temperature-Dependent Optical Properties

Temperature-dependent optical properties were only measured for the thick samples of the BIBO crystals. To obtain valid data on refractive indices and absorption coefficients, we considered the linear thermal expansion of the crystal. Linear thermal expansion coefficients were taken from [30]. Since the *y* dielectric axis lies between the *a* and *c* crystallographic axes, which have different signs of thermal expansion coefficients, the resulting thermal expansion of the *y*-cut sample is almost negligible. Cooling the sample down from room temperature to the liquid nitrogen (LN) temperature causes its length to increase by 6.3 μm, while heating from 22 to 200 °C leads to a length compression of 5.6 μm. As the *x* dielectric axis coincides with the *b* crystallographic axis, which has the highest linear expansion coefficient, the resulting expansion of the *x*-cut sample is more noticeable. Cooling the *x*-cut sample down to the LN temperature shrinks its length by 58 μm, while heating it to 200 °C leads to a 52 μm increase. Figure 3 shows the temperature dependencies of the absorption coefficients for all principal axes of the BIBO crystal.

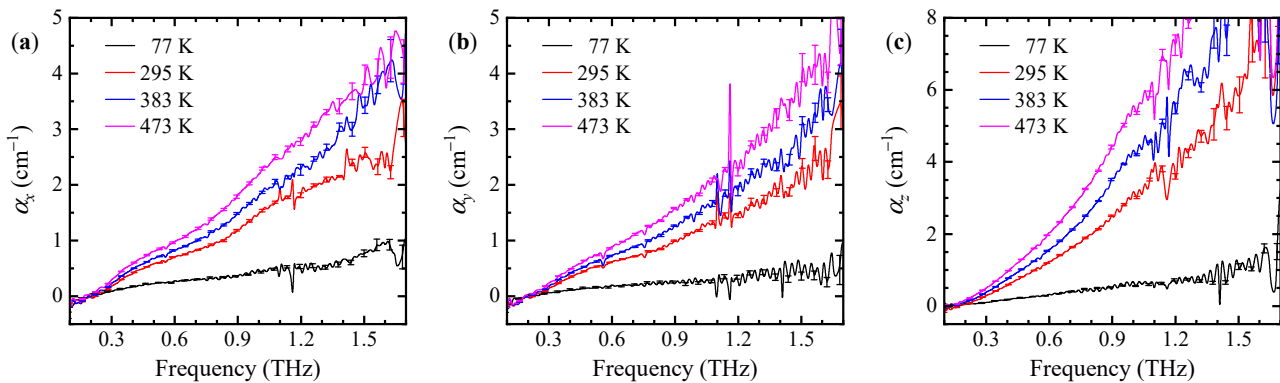


Figure 3. Absorption coefficient of the BIBO crystals in the THz range at different temperatures (77–473 K): (a) *x*-axis; (b) *y*-axis; (c) *z*-axis.

At longer wavelengths (>1500 μm), the absorption coefficients for all components are less than 0.1 cm⁻¹ and practically do not change with the temperature within the limits of measurement accuracy. Heating the samples leads to a small linear increase in the absorption coefficients in the short-wavelength region (<1500 μm or >0.2 THz). In this range, the absorption coefficients along the *z*-axis of the crystal are the largest (8 cm⁻¹ at 300 μm), while the absorption along the *x*- and *y*-axes is about 1.6 times lower. Additionally, cooling the samples down to 77 K at these wavelengths leads to a drastic decrease in absorption coefficients (from 8 to 10 times). This behavior can be described by an analogy with data on the temperature-dependent THz absorption of α-BBO crystal by Prof. X.-C. Zhang et al. [40]. According to this work, the phonon absorption peak at 2.5 THz becomes narrower and shifts to a higher frequency at a low temperature due to the Bose–Einstein distribution of vibrational modes. And vice versa, at higher temperatures, the center frequency of the phonon experiences a red shift while the peak width broadens. In the case of the BIBO crystal, the absorption is more likely caused by the low-frequency tail of a phonon peak. According to Raman spectroscopy, the center frequency of this peak should be located near 4.3 THz [41,42]. Unfortunately, the limited bandwidth of our THz-TDS does not allow us to reveal this phonon directly.

The temperature dependencies of the BIBO refractive indices are shown in Figure 4.

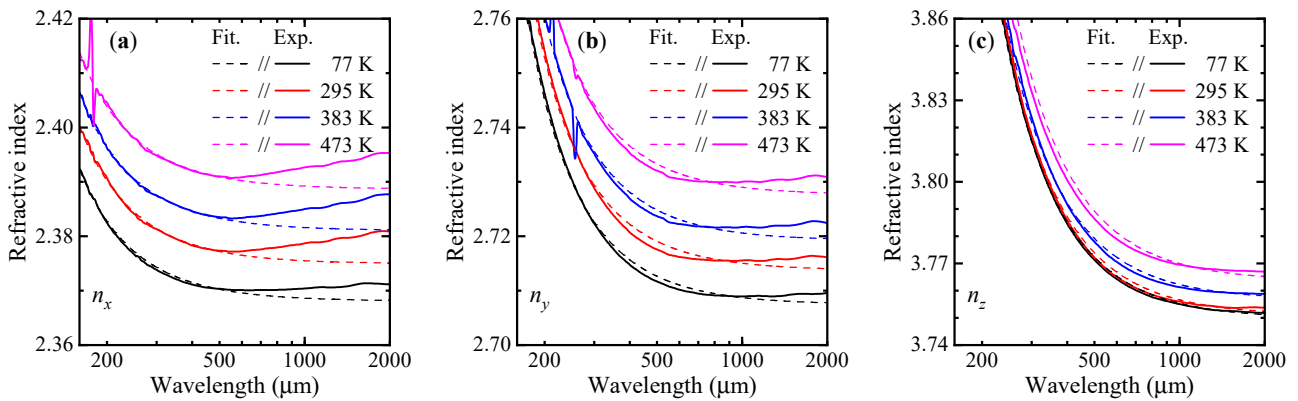


Figure 4. Experimentally measured and Sellmeier-fit refractive indices of the BIBO crystal in the THz range at different temperatures (77–473 K): (a) x -axis; (b) y -axis; (c) z -axis.

The long-wavelength tails of the refractive indices along the x - and y -axes decrease in proportion to the square of the temperature change upon cooling. The behavior of the refractive index along the z -axis is linear with respect to the temperature change. The upward deviation from the straight line of the long-wavelength tails of the refractive indices along the x - and y -axes may be related to diffraction in the thick samples, which is also confirmed by the presence of an interference pattern in the long-wavelength region of the absorption spectra in Figure 3a,b. Due to this fact, experimental points with a wavelength $> 1000 \mu\text{m}$ were omitted during the fitting process. Temperature-dependent Sellmeier coefficients were found in the vicinity of the values corresponding to the room temperature (1).

The temperature dependence of the fitted Sellmeier coefficients for all principal axes is shown in Figure 5 and Table 1.

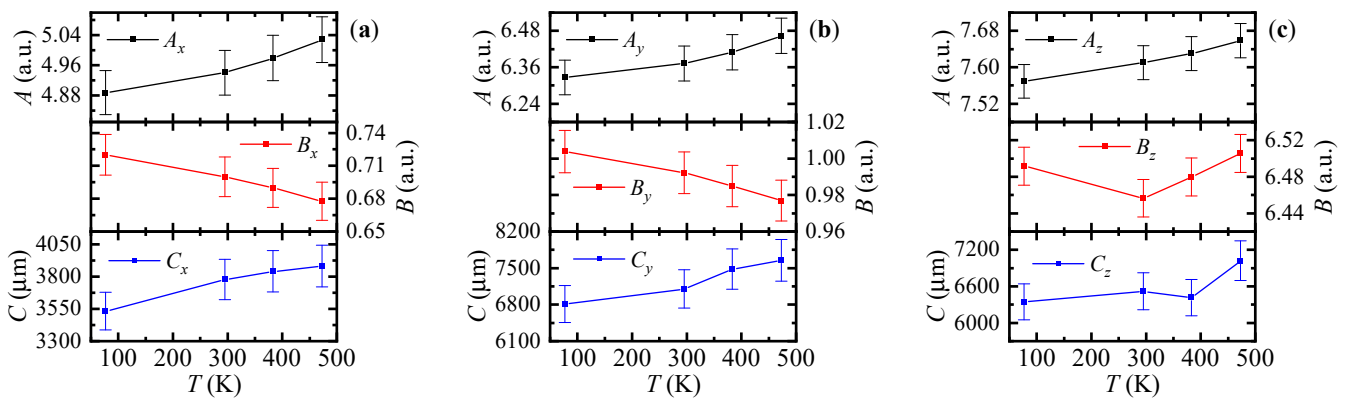


Figure 5. Temperature dependence of Sellmeier coefficients: (a) x -axis; (b) y -axis; (c) z -axis.

The temperature dependencies of the Sellmeier coefficients A_x and A_y were fitted with a quadratic polynomial, while for all other coefficients a linear fit was performed. The first derivatives of these coefficients with respect to the temperature are shown in Table 2.

Table 1. Sellmeier coefficients for different temperatures.

Principle Axis (n_i)	T (°C)	T (K)	A_i (a.u.)	B_i (a.u.)	C_i (μm^2)
n_x	−196	77	4.888	0.720	3532
	22	295	4.940	0.700	3777
	110	383	4.979	0.690	3841
	200	473	5.028	0.678	3881
n_y	−196	77	6.326	1.004	6808
	22	295	6.372	0.992	7100
	110	383	6.409	0.985	7477
	200	473	6.463	0.977	7646
n_z	−196	77	7.569	6.492	6345
	22	295	7.610	6.456	6515
	110	383	7.630	6.480	6410
	200	473	7.658	6.506	7020

Table 2. Form of temperature derivatives of the fitted Sellmeier coefficients.

Principle Axis (n_i)	$dA_i \times 10^5$ (K^{-1})	$dB_i \times 10^4$ (K^{-1})	dC_i ($\mu\text{m}^2 \cdot \text{K}^{-1}$)
n_x	$0.127 \cdot T + 0.69$	−1.053	0.91
n_y	$0.155 \cdot T - 8.30$	−0.667	2.16
n_z	21.9	0.214	1.33

As a result, we propose a form of dispersion equations as an integral function of T based on the corresponding temperature coefficients and their temperature derivatives:

$$n_i^2(T) = A_{i0} + \int_{T_0}^T dA_i dT + \frac{\left(B_{i0} + \int_{T_0}^T dB_i dT \right) \cdot \lambda^2}{\lambda^2 - \left(C_{i0} + \int_{T_0}^T dC_i dT \right)} \tag{2}$$

Such modified equations allow one to determine the refractive indices in the wavelength range of 150–3000 μm (0.1–2.0 THz) for any desired temperature in the range of 77–473 K. We suggest using the coefficients from the equations obtained at room temperature as the initial ones since they were derived from the combined experimental data of two different thicknesses of the BIBO samples, which makes them more accurate.

To determine the refractive index value at the pump wavelength, we used thermo-optics dispersion formulas presented in [43]. Although these formulas were only validated for a temperature range of 20 °C to 120 °C, their linear dependence allows us to estimate the refractive index at other temperatures as well.

The resulting equations enable the numerical calculation of the temperature-dependent PM conditions for the down-conversion of femtosecond laser radiation into the THz range. Finding such conditions, also known as birefringent phase matching, for fixed wavelengths is numerically equivalent to adjusting the refractive indices of the corresponding extraordinary waves according to the polar and azimuthal angles θ and φ in such a way as to zero the wavevector mismatch:

$$k_3 - k_2 - k_1 = 0$$

$$k_i(\lambda, T, \varphi, \theta) = 2\pi \cdot n_i^{(e,o)}(\lambda, T, \varphi, \theta) \cdot \lambda_i^{-1} \quad (3)$$

where λ_i and k_i are wavelengths in μm and wave vectors. In this case, k_3 and k_2 correspond to the pump and idler waves in the near-IR spectral range, and k_1 is a signal wave in the THz range ($\lambda_1 > \lambda_2 > \lambda_3$). Assuming the conversion of a broadband spectrum of the pump wave, for simplicity, we can fix λ_3 . Then, for any predetermined signal wavelength λ_1 it is possible to uniquely choose an idler wavelength λ_2 in the vicinity of λ_3 to fulfill the energy conservation condition:

$$\lambda_2 = \frac{\lambda_1 \lambda_3}{\lambda_3 + \lambda_1}. \quad (4)$$

It is necessary to keep in mind that all types of three-wave mixing processes can be realized in the case of down-conversion into the THz range, i.e., beyond the “Reststrahlen” band of the crystal, if the corresponding effective nonlinear coefficient is not equal to zero. For example, it was found that the mixing of three extraordinary waves in GaSe crystal leads to effective THz generation [44]. To avoid any misconduct, for BIBO being a biaxial crystal, we have chosen “slow” and “fast” notation for interacting waves instead of “ordinary” and “extraordinary”, generally used in the case of uniaxial crystals. For instance, in the case of three-wave mixing in the xz plane of a BIBO crystal for which the condition $n_z > n_y > n_x$ is satisfied both in the optical and THz ranges, the $k_1^e = k_3^e - k_2^e$ type of interaction should be denoted as $k_1^f = k_3^f - k_2^f$ when $\theta_{int} < V_z$ and as $k_1^s = k_3^s - k_2^s$ when $\theta_{int} > V_z$ [45], where V_z is an angle of the optical axes with the principal axis z .

The calculated wavevector mismatch for all three principal planes of BIBO is shown in Figure 6. Here, we choose $\lambda_1 = 1000 \mu\text{m}$ as a signal wavelength in the THz range and $\lambda_3 = 0.8 \mu\text{m}$ as a pump wavelength, corresponding to a Ti:sapphire femtosecond laser.

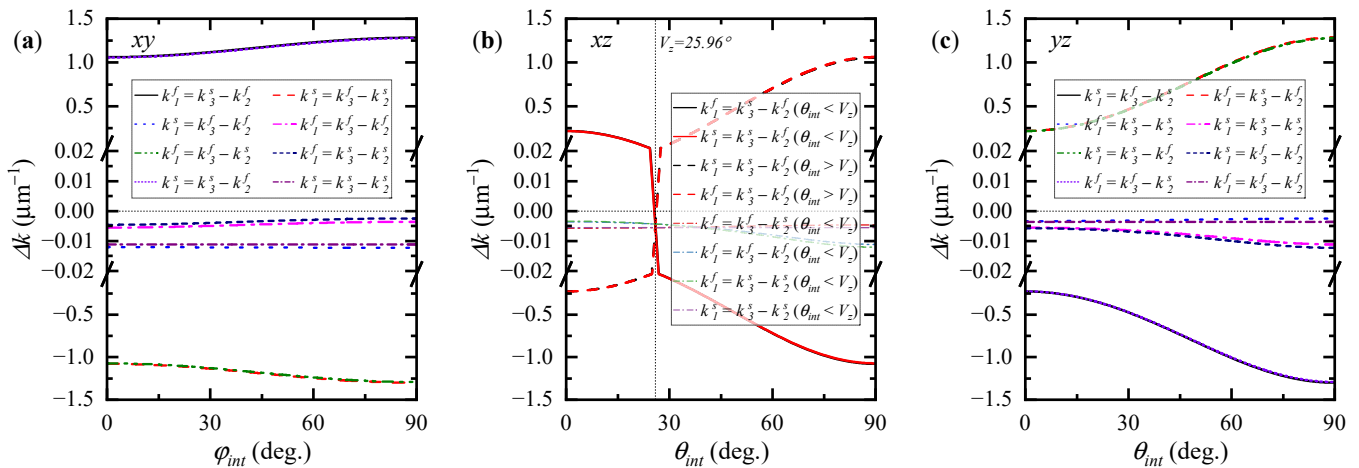


Figure 6. Wavevector mismatch for down-conversion into the THz range in the principal planes of BIBO crystal: (a) xy plane; (b) xz plane; (c) yz plane.

All types of wave interactions in the xy (Figure 6a) and yz (Figure 6c) principal planes exhibit a nonzero phase mismatch for $\lambda_1 = 1000 \mu\text{m}$ at any temperature considered. It indicates the non-fulfillment of the phase-matching conditions in these planes. On the other hand, calculations show that near the crystal optical axis in the xz principal plane, the PM conditions are satisfied for $s - f = f$ and $s - f = s$ mixing when $\theta_{int} < V_z$ and for $s - f = s$ and $s - f = f$ interactions when $\theta_{int} > V_z$ (Figure 6b). However, it should be noted that these types of frequency conversion are highly sensitive to changes in angle and possess an angular bandwidth $\Delta\theta$ of only 6 mrad for a 1 mm sample. In other words, even a slight rotation of the sample by 1° results in a PM frequency offset of 1.2 THz due to the large birefringence of the BIBO crystal. These four interactions turn out to be pairwise symmetric with respect

to the angle V_z . The values of the effective nonlinear coefficient d_{eff} corresponding to them are numerically identical in the same pairs [29]: $d_{eff} = -d_{14} \sin 2\theta$ for $s - f = f$ ($\theta_{int} < V_z$) and $s - f = s$ ($\theta_{int} > V_z$) types, and $d_{eff} = d_{12} \cos \theta$ for $s - f = s$ ($\theta_{int} < V_z$) and $s - f = f$ ($\theta_{int} > V_z$), assuming Kleinman symmetry due to close-to-zero absorption coefficients in the considered range.

4. Discussion

We have calculated temperature-tuning curves for the types of interactions involving PM in the xz plane. The dependence of the PM angles on λ_1 is shown in Figure 7a. The semi-transparent curves correspond to PM at the LN temperature and 473 K (200 °C). These curves are again pairwise symmetrical with respect to the V_z angle and follow it upon heating. The V_z changes from 26.8° to 25.2° when the crystal is heated from 77 K to 473 K. Figure 7b represents these changes at the wavelength of $\lambda_3 = 0.8 \mu\text{m}$ (dashed blue curve) and the corresponding temperature shift of the PM curves presented for the fixed signal wavelength at $\lambda_1 = 1000 \mu\text{m}$.

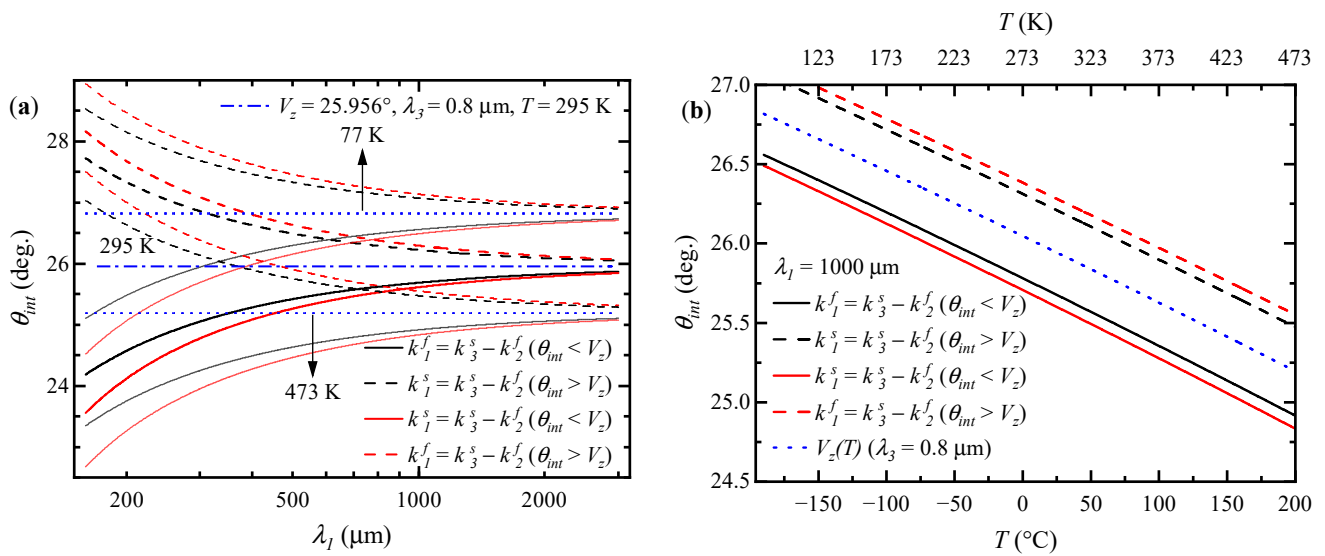


Figure 7. Temperature dependence of phase-matching conditions for the xz plane: (a) phase-matching angles for different signal wavelengths λ_1 ; (b) phase-matching angles for $\lambda_1 = 1000 \mu\text{m}$.

Let us consider a crystal cut with $\theta_{int} = 25.68^\circ$ and $\phi = 0^\circ$ which corresponds to the PM wavelength of $\lambda_1 = 1000 \mu\text{m}$ at room temperature. Temperature-tuning curves for this case are shown in Figure 8. Changing the crystal temperature makes it possible to tune the signal wavelength λ_1 over a wide spectral range. Varying the temperature from -50°C to 50°C , allows for access to the wavelength of 590–2165 μm (0.14–0.65 THz). However, for temperatures from 70°C to 106°C , the curves show quite a radical slope, which makes tuning almost unusable in real life since it requires the most precise temperature control. Moreover, in this case, the signal wavelength λ_1 shifts to the millimeter range or microwaves rather than the THz region.

In this case, the selected crystal cut has a “walk-off” angle ρ that does not exceed 60 mrad. Therefore, the effective aperture length L_a for a pump beam with a diameter of 1 mm is found to be more than 16 mm. Additionally, the coherence length for the optical rectification of femtosecond pulses generating THz radiation should be about 1 mm, according to [46]. Finally, these data allow us to simulate the resulting spectra of THz generation under a high-intensity pump. To simulate DFG THz spectra, we used a formula for the DFG conversion efficiency in the infinite plane wave under a non-depleted pump approximation, including the effects of the linear absorption from [23] and the values of corresponding nonlinearity tensors in the dielectric frame from [29]. Simulated DFG

THz spectra for a 5 mm thick PM cut crystal, as well as for an x-cut (*yz* plane) crystal of the same thickness under a $1 \text{ TW}\cdot\text{cm}^{-2}$ pump at 800 nm, at room temperature, are shown in Figure 9.

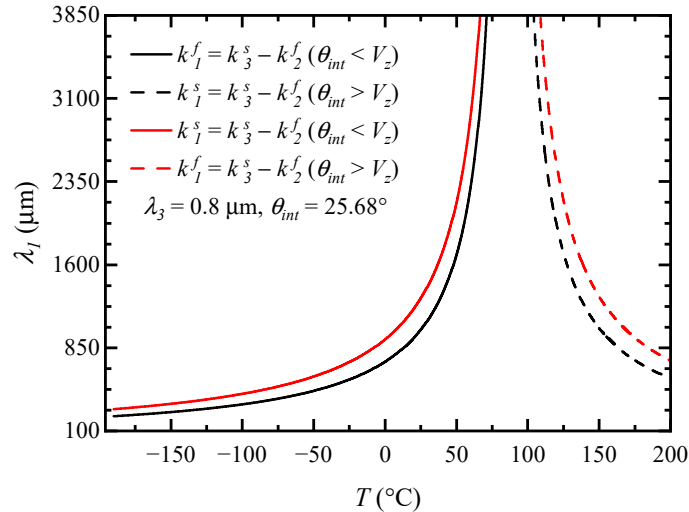


Figure 8. Temperature dependence of the phase-matching curves for the BIBO cut at $\theta_{int} = 25.68^\circ$ in the *xz* plane.

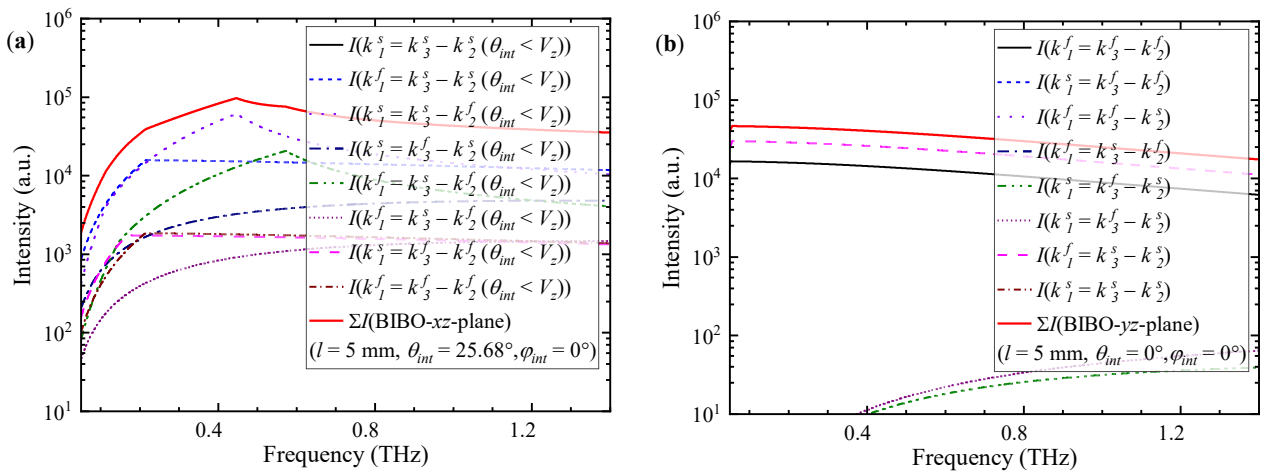


Figure 9. Simulation of terahertz generation by collinear three-wave mixing: (a) phase-matched cut crystal; (b) x-cut crystal.

The total intensity of the THz-generated spectra for the PM cut crystal (Figure 9a) shows two peaks corresponding to the PM interactions and a broad band substrate caused by optical rectification. The simulated intensities in these spectra are mostly limited by the effective lengths of the sample. In the case of PM interactions, the sample length limits the intensity, and in the case of optical rectification, the coherence length limits it. It is interesting to note that our calculations show that the total intensity of optical rectification in the x-cut sample is only one order of magnitude lower than the intensity of PM interaction in the PM cut crystal. Taking into account the high values of its nonlinear coefficients, it renders BIBO as one of the most prospective crystals of the borate family for phase- and non-phase-matched THz generation. The FOM for THz DFG in the BIBO crystal is estimated to be 1.5 times greater than that of the β -BBO crystal and almost 75 times greater than that of the LBO crystal.

5. Conclusions

In this research, we performed a thorough experimental study of the optical properties of the bismuth triborate nonlinear crystal in the range of 0.1–2.1 THz at temperatures from $-196\text{ }^{\circ}\text{C}$ to $200\text{ }^{\circ}\text{C}$. As a result, a new set of thermo-optic dispersion formulas was derived. We found that the BIBO crystal has nearly “zero” absorption coefficients below 0.33 THz; moreover, cooling it down to the LN temperature expands its transparency up to 1 THz. Our calculations on the PM conditions for collinear three-wave mixing processes providing efficient THz radiation generation allowed us to identify the optimal crystal cut. The PM conditions are fulfilled in the principal xz plane of the crystal for $\theta_{int} = 25.68^{\circ}$ at room temperature. Due to the narrow angular bandwidth of the DFG, we propose the use of temperature tuning for the PM frequency instead of crystal rotation. Varying the crystal temperature from $-50\text{ }^{\circ}\text{C}$ to $50\text{ }^{\circ}\text{C}$ corresponds to the frequency tuning range of 0.14–0.65 THz. Taking into account the smaller absorption coefficients of BIBO, this reveals its higher potential efficiency of THz nonlinear generation compared to the other crystals of the borate family. Despite the absence of the PM interactions in the xy and yz planes, the optical rectification coherence length for these planes is also in the range of 1 to 5 mm, making them viable for high-intensity frequency conversion into the THz range.

Author Contributions: Conceptualization, Y.A. and N.N.; methodology, N.N. and D.E.; software, D.E.; validation, V.A., Y.A. and V.S.; formal analysis, V.S.; investigation, D.E. and S.B.; resources, V.A.; data curation, D.E. and S.B.; writing—original draft preparation, D.E. and V.S.; writing—review and editing, D.E., Y.A. and N.N.; visualization, D.E.; supervision, Y.A. and V.S.; project administration, V.A.; funding acquisition, N.N. and Y.A. All authors have read and agreed to the published version of the manuscript.

Funding: The study was carried out within the framework of the State Assignment projects of Institute of Automation and Electrometry SB RAS (IA&E SB RAS), Institute of Laser Physics SB RAS, and Institute of Monitoring of Climatic and Ecological Systems SB RAS (IMCES SB RAS).

Institutional Review Board Statement: The study did not require ethical approval.

Informed Consent Statement: The study did not involve humans.

Data Availability Statement: Not applicable.

Acknowledgments: The authors express their gratitude to the Shared Equipment Center “Spectroscopy and Optics” of the IA&E SB RAS and the Shared Research Center “VTAN” of the Novosibirsk State University for the provided instrumental support.

Conflicts of Interest: The authors declare no conflict of interest. Funding organization had no role in the design of the study; in the collection, analyses, and interpretation of data; in the writing of the manuscript; and in the decision to publish the results.

References

1. Son, J.-H. *Terahertz: Biomedical Science & Technology*; CRC Press: Boca Raton, FL, USA, 2014; ISBN 9780367576127.
2. Chen, X.; Lindley-Hatcher, H.; Stantchev, R.I.; Wang, J.; Li, K.; Hernandez Serrano, A.; Taylor, Z.D.; Castro-Camus, E.; Pickwell-MacPherson, E. Terahertz (THz) biophotonics technology: Instrumentation, techniques, and biomedical applications. *Chem. Phys. Rev.* **2022**, *3*, 011311. [[CrossRef](#)]
3. Takida, Y.; Nawata, K.; Minamide, H. Security screening system based on terahertz-wave spectroscopic gas detection. *Opt. Express* **2021**, *29*, 2529–2537. [[CrossRef](#)]
4. Brown, E.R. Fundamentals of terrestrial millimeter-wave and THz remote sensing. *Int. J. High Speed Electron. Syst.* **2003**, *13*, 995–1097. [[CrossRef](#)]
5. Kim, G.-R.; Moon, K.; Park, K.H.; O'Hara, J.F.; Grischkowsky, D.; Jeon, T.-I. Remote N_2O gas sensing by enhanced 910-m propagation of THz pulses. *Opt. Express* **2019**, *27*, 27514. [[CrossRef](#)] [[PubMed](#)]
6. Liu, L.; Weng, C.; Li, S.; Husi, L.; Hu, S.; Dong, P. Passive remote sensing of ice cloud properties at terahertz wavelengths based on genetic algorithm. *Remote Sens.* **2021**, *13*, 735. [[CrossRef](#)]
7. Hwu, S.U.; Desilva, K.B.; Jih, C.T. Terahertz (THz) wireless systems for space applications. In Proceedings of the 2013 IEEE Sensors Applications Symposium Proceedings, Galveston, TX, USA, 19–21 February 2013; pp. 171–175. [[CrossRef](#)]
8. Huang, Y.; Shen, Y.; Wang, J. From Terahertz Imaging to Terahertz Wireless Communications. *Engineering* **2023**, *22*, 106–124. [[CrossRef](#)]

9. Naftaly, M.; Vieweg, N.; Deninger, A. Industrial Applications of Terahertz Sensing: State of Play. *Sensors* **2019**, *19*, 4203. [[CrossRef](#)]
10. Naftaly, M. Characterisation of Emitters and Detectors. In *Next Generation Wireless Terahertz Communication Networks*; CRC Press: Boca Raton, FL, USA, 2021; pp. 89–111, ISBN 9781003001140.
11. Ahn, J.; Efimov, A.; Averitt, R.; Taylor, A. Terahertz waveform synthesis via optical rectification of shaped ultrafast laser pulses. *Opt. Express* **2003**, *11*, 2486. [[CrossRef](#)]
12. Bernerd, C.; Segonds, P.; Debray, J.; Roux, J.-F.; Hérault, E.; Coutaz, J.-L.; Shoji, I.; Minamide, H.; Ito, H.; Lupinski, D.; et al. Evaluation of eight nonlinear crystals for phase-matched Terahertz second-order difference-frequency generation at room temperature. *Opt. Mater. Express* **2020**, *10*, 561–576. [[CrossRef](#)]
13. Lanin, A.A.; Voronin, A.A.; Stepanov, E.A.; Fedotov, A.B.; Zheltikov, A.M. Frequency-tunable sub-two-cycle 60-MW-peak-power free-space waveforms in the mid-infrared. *Opt. Lett.* **2014**, *39*, 6430. [[CrossRef](#)]
14. Hafez, H.A.; Chai, X.; Ibrahim, A.; Mondal, S.; Férachou, D.; Ropagnol, X.; Ozaki, T. Intense terahertz radiation and their applications. *J. Opt.* **2016**, *18*, 093004. [[CrossRef](#)]
15. Dong, Y.Q.; Yin, Y.; Huang, J.J.; Zhang, X.L.; Andreev, Y.M.; Ezhov, D.M.; Grechin, S.G. Optimization on the frequency conversion of LiGaS₂ crystal. *Laser Phys.* **2019**, *29*, 095403. [[CrossRef](#)]
16. Kokh, A.; Kononova, N.; Mennerat, G.; Villeval, P.; Durst, S.; Lupinski, D.; Vlezko, V.; Kokh, K. Growth of high quality large size LBO crystals for high energy second harmonic generation. *J. Cryst. Growth* **2010**, *312*, 1774–1778. [[CrossRef](#)]
17. Shi, W.; Ding, Y.J.; Fernelius, N.; Vodopyanov, K. Efficient, tunable, and coherent 0.18–5.27-THz source based on GaSe crystal. *Opt. Lett.* **2002**, *27*, 1454–1456. [[CrossRef](#)]
18. Rowley, J.D.; Wahlstrand, J.K.; Zawilski, K.T.; Schunemann, P.G.; Giles, N.C.; Bristow, A.D. Terahertz generation by optical rectification in uniaxial birefringent crystals. *Opt. Express* **2012**, *20*, 16958–16965. [[CrossRef](#)]
19. Lubenko, D.M.; Losev, V.F.; Andreev, Y.M.; Lanskii, G.V. Model studies of THz-range generation via down conversion of the radiation of Ti:Sapphire lasers in LBO crystals. *Bull. Russ. Acad. Sci. Phys.* **2017**, *81*, 1239–1243. [[CrossRef](#)]
20. Mamrashev, A.; Nikolaev, N.; Antsygin, V.; Andreev, Y.; Lanskii, G.; Meshalkin, A. Optical properties of KTP crystals and their potential for Terahertz generation. *Crystals* **2018**, *8*, 310. [[CrossRef](#)]
21. Lubenko, D.M.; Lansky, G.V.; Nikolaev, N.A.; Sandabkin, E.A.; Losev, V.F.; Andreev, Y.M. Generation of THz emission in nonlinear BBO crystal at room temperature. In Proceedings of the XIV International Conference on Pulsed Lasers and Laser Applications, Tomsk, Russia, 15–20 September 2019; SPIE: Bellingham, Washington, USA, 2019; Volume 11322, pp. 498–503.
22. Rybak, A.; Antsygin, V.; Mamrashev, A.; Nikolaev, N. Terahertz optical properties of KTiOPO₄ crystal in the temperature range of (−192)–150 °C. *Crystals* **2021**, *11*, 125. [[CrossRef](#)]
23. Sutherland, R.L. *Handbook of Nonlinear Optics*; CRC Press: Boca Raton, FL, USA, 2003; ISBN 9781135541194.
24. Hellwig, H.; Liebertz, J.; Bohaty, L. Exceptional large nonlinear optical coefficients in the monoclinic bismuth borate BiB₃O₆ (BIBO). *Solid State Commun.* **1999**, *109*, 249–251. [[CrossRef](#)]
25. Kroupa, J.; Kasprowicz, D.; Majchrowski, A.; Michalski, E.; Drozdowski, M. Optical properties of Bismuth Triborate (BIBO) single crystals. *Ferroelectrics* **2005**, *318*, 77–82. [[CrossRef](#)]
26. Jang, J.H.; Yoon, I.H.; Yoon, C.S. Cause and repair of optical damage in nonlinear optical crystals of BiB₃O₆. *Opt. Mater.* **2009**, *31*, 781–783. [[CrossRef](#)]
27. Apurv Chaitanya, N.; Aadhi, A.; Singh, R.P.; Samanta, G.K. Type-I frequency-doubling characteristics of high-power, ultrafast fiber laser in thick BIBO crystal. *Opt. Lett.* **2014**, *39*, 5419–5422. [[CrossRef](#)]
28. Galletti, M.; Pires, H.; Hariton, V.; Alves, J.; Oliveira, P.; Galimberti, M.; Figueira, G. Ultra-broadband near-infrared NOPAs based on the nonlinear crystals BiBO and YCOB. *High Power Laser Sci. Eng.* **2020**, *8*, e29. [[CrossRef](#)]
29. Petrov, V.; Ghotbi, M.; Kokabee, O.; Esteban-Martin, A.; Noack, F.; Gaydardzhiev, A.; Nikolov, I.; Tzankov, P.; Buchvarov, I.; Miyata, K.; et al. Femtosecond nonlinear frequency conversion based on BiB₃O₆. *Laser Photon. Rev.* **2010**, *4*, 53–98. [[CrossRef](#)]
30. Bubnova, R.; Volkov, S.; Albert, B.; Filatov, S. Borates—Crystal Structures of Prospective Nonlinear Optical Materials: High Anisotropy of the Thermal Expansion Caused by Anharmonic Atomic Vibrations. *Crystals* **2017**, *7*, 93. [[CrossRef](#)]
31. Li, Y.; Huang, J.; Huang, Z.; Nikolaev, N.; Lanskii, G.; Mamrashev, A.; Andreev, Y. Optical properties of BiB₃O₆ in the terahertz range. *Results Phys.* **2020**, *16*, 102815. [[CrossRef](#)]
32. Nikolaev, N.A.; Mamrashev, A.A.; Antsygin, V.D.; Ezhov, D.M.; Lubenko, D.M.; Svetlichnyi, V.A.; Andreev, Y.M.; Losev, V.F. Millimetre-wave range optical properties of BIBO. *J. Phys. Conf. Ser.* **2021**, *2067*, 012011. [[CrossRef](#)]
33. Ghorui, C.; Rudra, A.M.; Chatterjee, U.; Chaudhary, A.K.; Ganesh, D. Efficient second-harmonic and terahertz generation from single BiB₃O₆ crystal using nanosecond and femtosecond lasers. *Appl. Opt.* **2021**, *60*, 5643–5651. [[CrossRef](#)] [[PubMed](#)]
34. Tzankov, P.; Petrov, V. Effective second-order nonlinearity in acentric optical crystals with low symmetry. *Appl. Opt.* **2005**, *44*, 6971–6985. [[CrossRef](#)]
35. Mamrashev, A.; Minakov, F.; Maximov, L.; Nikolaev, N.; Chapovsky, P. Correction of Optical Delay Line Errors in Terahertz Time-Domain Spectroscopy. *Electronics* **2019**, *8*, 1408. [[CrossRef](#)]
36. Mamrashev, A.A.; Nikolaev, N.A.; Kuznetsov, S.A.; Gelfand, A.V. Broadband metal-grid polarizers on polymeric films for terahertz applications. In *AIP Conference Proceedings, Proceedings of the 5th International Conference on Metamaterials and Nanophotonics Metanano 2020, St. Petersburg, Russia, 14–18 September 2020*; AIP Publishing LLC: Melville, NY, USA, 2020; Volume 2300, p. 020083.
37. Mamrashev, A.; Minakov, F.; Nikolaev, N.; Antsygin, V. Terahertz Time-Domain Polarimetry for Principal Optical Axes of Anisotropic Crystals. *Photonics* **2021**, *8*, 213. [[CrossRef](#)]

38. Duvillaret, L.; Garet, F.; Coutaz, J.-L. A reliable method for extraction of material parameters in terahertz time-domain spectroscopy. *IEEE J. Sel. Top. Quantum Electron.* **1996**, *2*, 739–746. [[CrossRef](#)]
39. Naftaly, M. *Terahertz Metrology*; Naftaly, M., Ed.; Artech House: Boston, MA, USA; London, UK, 2015; ISBN 9781608077779.
40. Liu, J.; Zhang, X.C. Birefringence and absorption coefficients of alpha barium borate in terahertz range. *J. Appl. Phys.* **2009**, *106*, 023107. [[CrossRef](#)]
41. Xia, H.R.; Li, L.X.; Teng, B.; Zheng, W.Q.; Lu, G.W.; Jiang, H.D.; Wang, J.Y. Raman scattering from bismuth triborate. *J. Raman Spectrosc.* **2002**, *33*, 278–282. [[CrossRef](#)]
42. Kasprowicz, D.; Runka, T.; Szybowicz, M.; Ziobrowski, P.; Majchrowski, A.; Michalski, E.; Drozdowski, M. Characterization of bismuth triborate single crystal using Brillouin and Raman spectroscopy. *Cryst. Res. Technol.* **2005**, *40*, 459–465. [[CrossRef](#)]
43. Umemura, N.; Miyata, K.; Kato, K. New data on the optical properties of BiB₃O₆. *Opt. Mater.* **2007**, *30*, 532–534. [[CrossRef](#)]
44. Nazarov, M.M.; Sarkisov, S.Y.; Shkurinov, A.P.; Tolbanov, O.P. Efficient terahertz generation in GaSe via eee-interaction type. In Proceedings of the 2011 International Conference on Infrared, Millimeter, and Terahertz Waves, Houston, TX, USA, 2–7 October 2011; pp. 1–2.
45. Powers, P.E. *Field Guide to Nonlinear Optics*; SPIE: Bellingham, WA, USA, 2013; ISBN 9780819496362.
46. Schneider, A.; Neis, M.; Stillhart, M.; Ruiz, B.; Khan, R.U.A.; Günter, P. Generation of terahertz pulses through optical rectification in organic DAST crystals: Theory and experiment. *J. Opt. Soc. Am. B* **2006**, *23*, 1822–1835. [[CrossRef](#)]

Disclaimer/Publisher’s Note: The statements, opinions and data contained in all publications are solely those of the individual author(s) and contributor(s) and not of MDPI and/or the editor(s). MDPI and/or the editor(s) disclaim responsibility for any injury to people or property resulting from any ideas, methods, instructions or products referred to in the content.